Construction and Building Materials 222 (2019) 829–838

Contents lists available at ScienceDirect

Construction and Building Materials

journal homepage: www.elsevier.com/locate/conbuildmat

# A new method for CF morphology distribution evaluation and CFRC property prediction using cascade deep learning

Zheng Tong [a,b], Jie Gao [c,*], Zhenjun Wang [d,*], Yongfeng Wei [a], Hui Dou [a]

[a] *Research and Development Center of Transport Industry of Technologies, Materials and Equipments of Highway Construction and Maintenance (Gansu Road & Bridge Construction Group), Lanzhou 730030, Gansu, PR China*
[b] *Sorbonne Université, Université de Technologie de Compiègne, CNRS, UMR 7253 Heudiasyc, CS 60319-60203 Compiègne Cedex, France*
[c] *School of Highway, Chang'an University, Xi'an 710064, PR China*
[d] *School of Materials Science and Engineering, Chang'an University, Xi'an 710061, PR China*

## HIGHLIGHTS

- A deep-learning method was proposed to characterize CF distribution and predict CFRC properties.
- High-precision 3D reconstruction using CT images and FCNs was conducted.
- The cascade deep learning predicted the CFRC properties using X-ray scanning images.
- The method measured the contributions of different CF distribution to CFRC properties.

## GRAPHICAL ABSTRACT

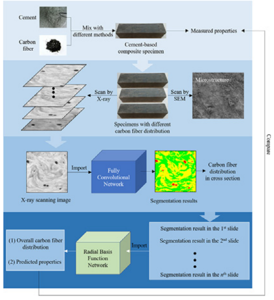

## ARTICLE INFO

*Article history:*
Received 16 April 2019
Received in revised form 9 June 2019
Accepted 20 June 2019
Available online 3 July 2019

*Keywords:*
Carbon fiber reinforced cement-based composites
Carbon fiber distribution
Computed tomography
Deep learning
Radial basis function network

## ABSTRACT

This work presents a deep-learning method to characterize the carbon fiber (CF) morphology distribution in carbon fiber reinforced cement-based composites (CFRC), predict the CFRC properties, and measure the contributions of different CF morphology distribution directly using X-ray images. Firstly, the components of CFRC in slices of X-ray images were segmented and identified using a fully convolutional network (FCN). Then the CF morphology distribution evaluation were conducted based on the results of the FCN. At last, the prediction of CFRC properties was realized using a cascade deep learning algorithm and CF morphology distribution results. The results showed that the FCN provided more reasonable segmentation results for each component in CFRC than traditional methods. CF clustered areas and CF bundles increased sharply with the increase of CF content, while uniformly dispersed CF areas showed the opposite trend. The cascade deep learning provided a method to predict the CFRC properties (e.g. resistivity and bending strength) using X-ray scanning images, which could also quantificationally measure the contributions of different CF morphology distribution to properties of the CFRC. Therefore, the proposed method could be regarded as a nondestructive and effective test for CFRC property evaluation.

## 1. Introduction

Carbon fiber reinforced cement-based composites (CFRC) hold prospect for future civil engineering because of their excellent mechanical [1], electrical [2], and thermal properties [3]. They have been proven that the effectiveness of the CFRC properties depends

---

* Corresponding authors.
*E-mail addresses:* zjwang@chd.edu.cn (Z. Wang), highway-gaojie@st.chd.edu.cn (J. Gao).

https://doi.org/10.1016/j.conbuildmat.2019.06.160

on the carbon fiber (CF) morphology distribution [4]. Consequently, a method for evaluating CF distribution quantitatively is essential to guarantee the excellent properties of CFRC.

A widely-used method for fiber distribution evaluation has been introduced in ASTM C1229-94 [5]. However, the traditional method only analyzes the fiber distribution indirectly and provides little information about the distribution morphology and volumes of different components [6]. Motivated by the disadvantages of the issue, many studies contributed to characterizing the CF distribution in the recent decades, such as scanning electron microscope (SEM), empirical equations, and X-ray computed tomography (CT). The SEM method is always used as an auxiliary evolution method because of its insensitive capacity to small differences in the degree of object characteristics evaluation due to the limited observation areas [7]. It is also unacceptable to evaluate the CF morphology distribution using empirical equations based on physical or mechanical properties [8] because a range of applicable conditions usually limit these empirical equations. Additionally, the determination of empirical constants is not easy to obtain and vary from one condition to another. Compared with these methods, the X-ray CT technique has the advantage to present the CF morphology distribution. With the development of industrial CT machines, it is no longer challenging to obtain sectional X-ray images [9]. However, there is still two problem limiting the utilization of X-ray images to evaluate the CF morphology distribution: (a) How to segment different components accurately (e.g. CF bundles, CF clustered areas, and uniformly dispersed CF areas) in the X-ray images; (b) However to build a relationship between the CF morphology distribution and CFRC properties.

Many methodologies were used to segment different components of CFRC in X-ray images. A widely-used method for the task is K-mean clustering. Comparing with the previous studies using this method [9,10], it could be found that the gray thresholds in the X-ray images varied not only from one specimen to another but also from one slide to another. It was owing to different densities and mass ratios of components in different specimens [11]. Additionally, many other techniques, such as density-gradients clustering [12], belief function fusion [13], random forest classifier [14], were used to complete the task but the results were also not reasonable. In one word, the features of different components in CFRC were not easily summarized accurately by a few indexes or equations, such as gray thresholds. Therefore, these traditional methodologies, which relied on humans to provide features of different components, were not suitable to segment X-ray images and evaluate the CF morphology distribution.

In recent years, the development of deep learning offers us a feasible option to realize the task. After the remarkable performance of the LeNet-5 [15,16], deep learning has been widely used in object classification [17,18], location [19,20], and segmentation [21,22]. Notably, a modified convolutional neural network (ConvNet), named fully convolutional network (FCN), shows excellent performance in object segmentation using X-ray images. For example, Xu et al. [23] segmented lung parenchyma in X-ray images successfully using an FCN. Zhang et al. [24] proposed an FCN to detect lesion using X-ray and magnetic resonance images. Tumor co-segmentation in PET/CT was realized using FCNs [25]. Therefore, it is possible to employee an FCN to segment different components in CFRC X-ray images. Additionally, deep-learning methods have been used to evaluate and predict material properties. For example, Liu et al. [26] proposed a region deep-learning method to locate carbon powder bunches and compute the carbon powder distribution of the modified asphalt using microscope images. Cang et al. [27] predicted physical properties of heterogeneous materials from imaging data via ConvNet. Jiang et al. [28] segmented different components in asphalt mixtures based on ConvNet using X-ray images but the proposed method was still influenced by the selection of gray thresholds. The previous studies indicated that deep learning methods might have the capacity to build a relationship between the CF morphology distribution and CFRC properties. Thus, it is a preferable choice to utilize FCN to segment different components of CFRC in X-ray images and use the results to characterize the CF morphology distribution.

In this study, motivated by the drawback of the CF distribution evolution methods in the previous study [8,9], we proposed a cascade deep learning method to characterize the CF morphology distribution and CFRC properties using X-ray images. The advantages of this study are summarized below:

(1) The proposed method provided stable and precisive segmentation results of X-ray images, which could be used to characterize the CF distribution accurately, such as distribution morphology and volumes of different components.
(2) The proposed method provided a way to build a relationship between the CF distribution and CFRC properties. The CF distribution was its real morphology distribution in the CFRC rather than the mass of CFs in a specimen. It provided a bridge between the CF morphology distribution and the property prediction in a nondestructive and effective mode.
(3) The proposed method could quantificationally evaluate the contributions of the different CF morphology distribution to the CFRC properties.

The rest of this paper is organized as follows. In Section 2, we present the method to prepare the CFRP specimens, acquire X-ray scanning images, and measure the resistivity and bending strength of each specimen. In Section 3, we descript the structure of the cascade deep learning, which combine an FCN and a radial basis function (RBF) network. In Section 4, we discuss the results of X-ray image segmentation, carbon fiber distribution evaluation, and a way to predict CFRC properties and evaluate the contributions of the different CF morphology distribution to the CFRC properties quantificationally. Our conclusions are summarized in Section 5.

## 2. Laboratory experiments

### 2.1. Raw materials

There were three kinds of raw materials involved in a CFRC specimen, ordinary Portland cement, short-cut CFs, and mixing water. Tables 1 and 2 present the properties of cement and CFs used in this study. The properties of the cement met the demands of GB 175-2007 [29].

### 2.2. Preparation of CFRC specimens

To acquire X-ray images with different CF morphology distribution, CFRC specimens were designed with three carbon fiber contents: 0.4%, 0.8%, and 1.2% of cement mass, respectively. These specimens were labeled as CF4, CF8, and CF12, respectively. The mass ratio of water in all CFRC specimens was 0.33. The after-mixing method was used to prepare all the specimens, which mean that the CFs were added into the mixture after preparing cement mortar. Detailed procedures have been presented in the study of Yang [30]. Firstly, the ordinary Portland cement and the mixing water were stirred by a cement mortar mixer in 60 round/min. The stirring time was 30 s. Secondly, CFs were added into the cement mortar. The stirring time was 120 s. Lastly, the cement mortar with CFs was infused into 40 mm × 40 mm × 160 mm models and cured in a condition where the temperature and relative humidity were controlled in 20 ± 2 °C and 93%, respectively.

**Table 1**
Cement properties.

| Fineness ($m^2$/kg) | Density (g/$cm^3$) | Initial/finial setting time (h) | Flexural/compressive strength (MPa) | |
|---|---|---|---|---|
| | | | 3 d | 28 d |
| 320 | 3.108 | 3.0/4.8 | 5.8/20.5 | 7.4/54.3 |

**Table 2**
Carbon fiber properties.

| Radius (μm) | Lengths (mm) | Carbon content (%) | Elasticity modulus (GPa) | Ultimate Tensile strength (MPa) | Resistivity ($10^{-3}$ Ω·cm) |
|---|---|---|---|---|---|
| 4.0 | 2–5 | 95.6 | 235 | 3900 | 0.783 |

After 28 days, the specimens were used to acquire X-ray images by an industrial CT machine, measure mechanical and electrical properties, and observe the microscopic distribution of CFs by scanning electron microscope (SEM). Three specimens were prepared for each carbon fiber content.

### 2.3. X-ray scanning

The specimens were dried 6 h before the X-ray scanning to acquire high-quality images. The procedures of X-ray scanning and the detailed information of the X-ray CT equipment are presented in Fig. 1. The resolution of the CFRC images depended on two indexes: spatial resolution and contrast resolution. The smallest size shown in an X-ray image is determined by the spatial resolution, while the capacity for distinguishing the smallest density between different components in the specimens was determined by the contrast resolution. In this study, the spatial and contrast resolution was 23 lp/mm and 0.2% to meet the demand of observing CF bundles, CF clustered areas, and uniformly dispersed CF areas. The scanning interval was 0.01 mm. Thus, 16,000 X-ray images were acquired by scanning a specimen with a 160 mm height. The massive X-ray images were used to generate a database for the cascade deep learning.

### 2.4. Measurement for CFRC properties

(1) Resistivity. A piece of self-made equipment was used to measure the resistivity of each specimen. Two copper sheets with 38 mm × 38 mm × 0.5 mm size were used as electrodes. To guarantee the precision of the resistivity measurement, the two sheets were bonded to two sides of a specimen using graphite-based epoxy conductive adhesive. One end of a wire was linked with the specimen, while another end was connected with a regulated power supply. The voltage was 30 V during the measurement. The current values were recorded and used to compute the resistance by Eq. (1).

$$\rho = \frac{Rs}{L} \tag{1}$$

where $\rho$ and $R$ are the resistivity and resistance, respectively; $s$ is the areas of two copper sheets; $L$ is the specimen length.

(2) Bending strength. The bending strengths were measured using a material testing system. The loading rate was controlled in 0.05 mm/s. The distance between the loading and each support was 50 mm, while the distance between a support and a specimen top was 30 mm.

### 2.5. Microscopic observation

A microscopic observation using a Hitachi S-4800 SEM was adopted to analyze fracture surface characteristics in CFRC specimens after the X-ray scanning and the property measurement. The observation results were assisted to determine the CF bundles, CF clustered areas, and uniformly dispersed CF areas in different X-ray images precisely, which improved the precision of the labels in the FCN database.

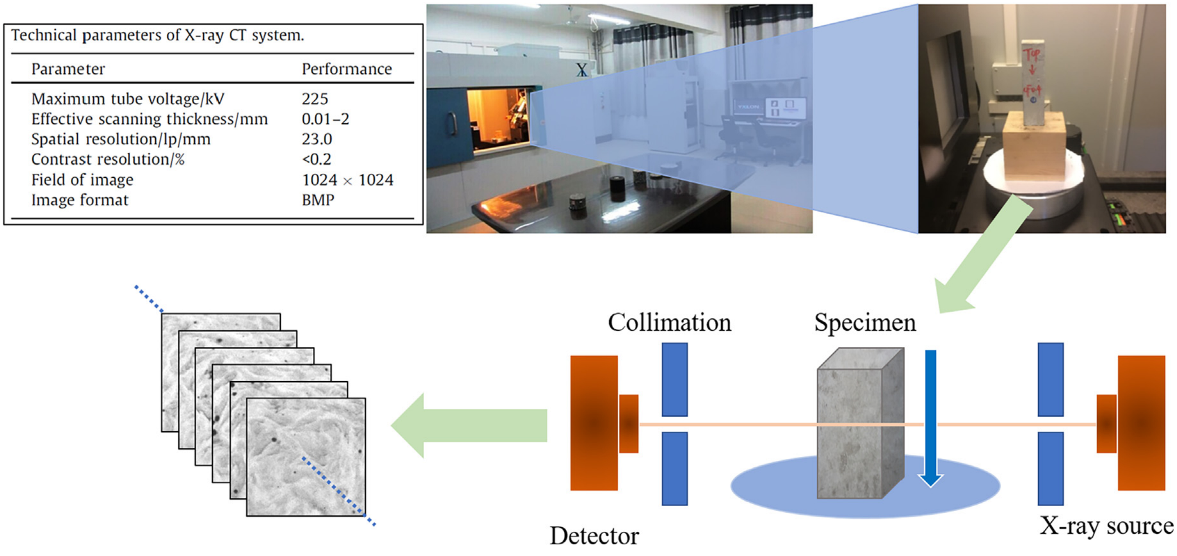

Technical parameters of X-ray CT system.

| Parameter | Performance |
|---|---|
| Maximum tube voltage/kV | 225 |
| Effective scanning thickness/mm | 0.01–2 |
| Spatial resolution/lp/mm | 23.0 |
| Contrast resolution/% | <0.2 |
| Field of image | 1024 × 1024 |
| Image format | BMP |

**Fig. 1.** X-ray scanning procedures.

## 3. Cascade deep learning

In this section, we first recall the fundamental theories of ConvNet in Section 3.1. We then provide descriptions of the FCN for segmenting different components in X-ray images in Section 3.2. At last, a cascade connection using an RBF network is proposed to predict the properties of CFRC in Section 3.3.

### 3.1. Fundamental theories of convolution neural network

Prior to the development of the FCN and its cascade connection using an RBF network, the fundamental theories with respect to ConvNet are recalled in this section briefly. Detailed information of these structural layers has been shown in the Refs. [16,31]. The structure layers from a traditional ConvNet used to build an FCN including convolutional layers and pooling layers.

Convolutional layer, as the key layer of a ConvNet, consists of many kernels to extract features related to the aim, such as segmenting objects in X-ray images. A kernel can be regarded as a feature extractor with learned connection weights to extract a certain feature from the input data. The processes of the feature extraction in a kernel can be summarized as Eq. (2). In general, a convolution layer with numbers of kernels extracts low-, medium-, or high-features from the input data. The extracted features are used to classify and segment objects.

$$z^{l}_{\mu,v} = \sum_{i=-\infty}^{+\infty} \sum_{j=-\infty}^{+\infty} x^{l-1}_{\mu,v} \cdot k^{l}_{rot_{i,j}} \cdot \chi(i,j) + b^{l} \tag{2a}$$

$$\chi(i,j) = \begin{cases} 1, 0 \leqslant i,j \leqslant n \\ \quad 0, other \end{cases} \tag{2b}$$

$$x^{l}_{\mu,v} = \frac{1}{1 + e^{z^{l-1}_{\mu,v}}} \tag{2c}$$

where, $x^{l}_{\mu,v}$ and $\times\, {}^{l}{}_{\mu}{}^{-}{}^{1}{}_{,v}$ are the output and input of the element in the $\mu$th row and $v$th column in the $l$th convolutional layer by the convolution operation of a kernel $k^{l}_{i,j}$. $k^{l}_{roti,j}$ is the transposed matrix of a kernel $k^{l}_{i,j}$. $b^{l}$ is the bias in the $l$th convolutional layer.

Pooling layer is utilized to decrease the spatial size of its input to reduce the computational costs and the possibility of the overfitting. Compared with traditional humble pooling operations, such as max-pooling and mean-pooling, which are blamed for the negative influence on object classification and segmentation [32], a stochastic pooling is adopted in this study [33]. A stochastic pooling is summarized as Eq. (3).

$$p_i = \frac{s^{l}_{\mu,v,i}}{\sum s^{l}_{\mu,v}} \tag{3a}$$

$$x^{l\,+\,1}_{\mu,v,i} = s^{l}_{\mu,v,l}\, where \quad l \sim P(p_1, \ldots, p_l, \ldots p_S) \tag{3b}$$

where $s^{l}_{\mu,v}$ is a subarray of the input array of the $(l+1)$th convolutional layer; $s^{l}_{\mu,v}$ is the $i$th element of the subarray; $s^{l+1}_{\mu,v}$ ,$i$ is the output results of the subarray.

### 3.2. Fully convolution network

A traditional ConvNet can only recognize different objects in an image but cannot define object areas owing to fully connected layers following the last convolutional or pooling layer. A fully connected layer is used to extend feature maps generated by the last convolutional or pooling layers to a vector and map it to a given space. The mapped vector is the probability scores of different objects. After the extension, the spatial features in feature maps are lost and the vector cannot be used to segment different objects. Therefore, we replace the fully connected layers with deconvolutional layers to realize the segmentation task. The modified ConvNet is called FCN as shown in Fig. 2.

The deconvolution can be regarded as a backwards strided convolution. The processes of deconvolution are summarized as Eq. (4),

$$y^{i}_{u+1} = \sum_{k=1}^{K} z^{i}_{u,k} \oplus f^{u}_{k,c} \tag{4}$$

where, $y^{i}_{u+1}$ and $z^{i}_{u}$ were the output and input of the $u$th deconvolutional layer, respectively. $K$ and $c$ were the numbers of kernels and feature maps in the $u$th deconvolutional layer. $f$ stood as a weight matrix of kernels in the $u$th deconvolutional layer. $\oplus$ stands as a deconvolutional operation. Detailed information of the deconvolution operation can be found in the study of Long et al [34]. Deconvolution operation in a $d \times d \times K$ deconvolution kernel with a fractional input stride of $1/d$ in height and width and $1/K$ in depth. As $d$ and $K$ are a positive integer, a natural way to deconvolution is backwards convolution with an output stride of $d$ and $K$.

The FCN used to segment CF bundles, CF clustered areas, and uniformly dispersed CF areas from X-ray images was realized by training using a stochastic gradient descent algorithm [35]. The aim of the training was to minimize the errors between the output segmentation results and ground truths. The errors were computed using an average binary cross entropy loss of each pixel in an image by Eq. (5). To minimize the errors, a database was generated including 11,200 high-quality X-ray images from 9 specimens with three carbon fiber contents: 0.4%, 0.8%, and 1.2%, respectively. We selected 6,720 and 2,240 X-ray images as the training set and validation set. The rest images were used as the testing set. Considering that the precision of labels in the database influenced the error minimizing, X-ray images were labeled with the assistance of SEM images as shown in Fig. 3.

$$Error = -\sum_{i=1}^{n} y'_i \log f(z_i) \tag{5a}$$

$$f(z_k) = \frac{e^{z_k - m}}{\sum_{i=1}^{n} e^{z_i - m}} \tag{5b}$$

The learning rate was 1e-4 in the study to guarantee that the weights of convolution and deconvolution kernels were not adjusted sharply. We set max 40 epochs for 100 training samples to prevent overfitting. The above procedure was performed in a Python environment on a computer equipped with an Intel(R) Core (TM) i7-8750H CPU, 32.00 GB RAM, and an NVIDIA GeForce GTX 1080 8 GB GPU.

### 3.3. Cascade connection using RBF network

The previous studies [9,10] showed that the CF distribution could be defined based on the segmentation results of all X-ray images from one specimen using different equations directly. However, it was difficult to predict CFRC properties (e.g. resistivity and bending strength) just using empirical equations based on the CF morphology distribution because different CF distribution in different slides of specimens made a different contribution to the CFRC properties, which was difficult to be defined by humans. Thus, we proposed a radial basis function (RBF) network to predict CFRC properties based on the outputs of the FCN. The proposed method for predicting CFRC properties by combining the FCN and the RBF network could be regarded as a cascade deep learning.

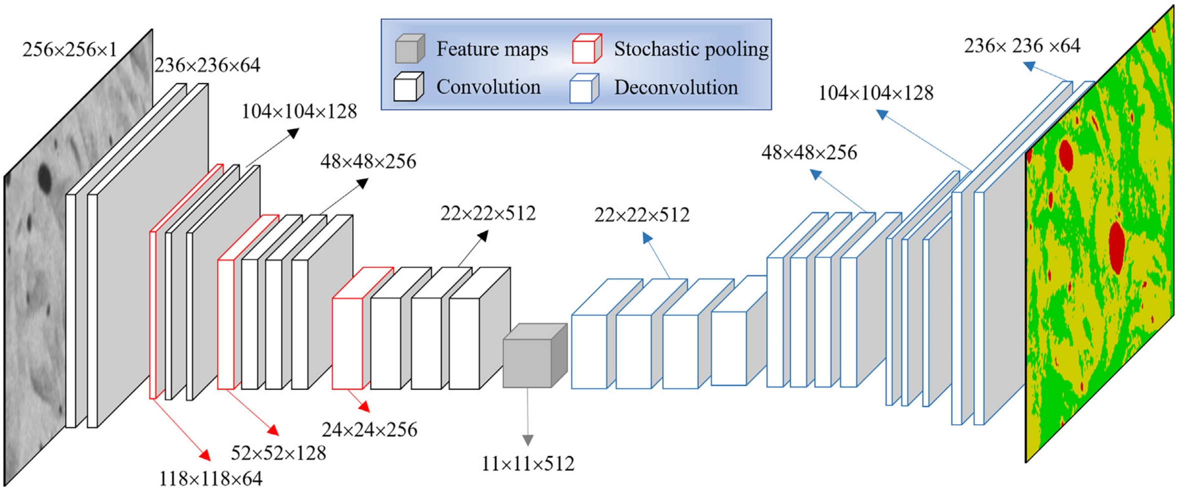

**Fig. 2.** Structure of fully convolutional network.

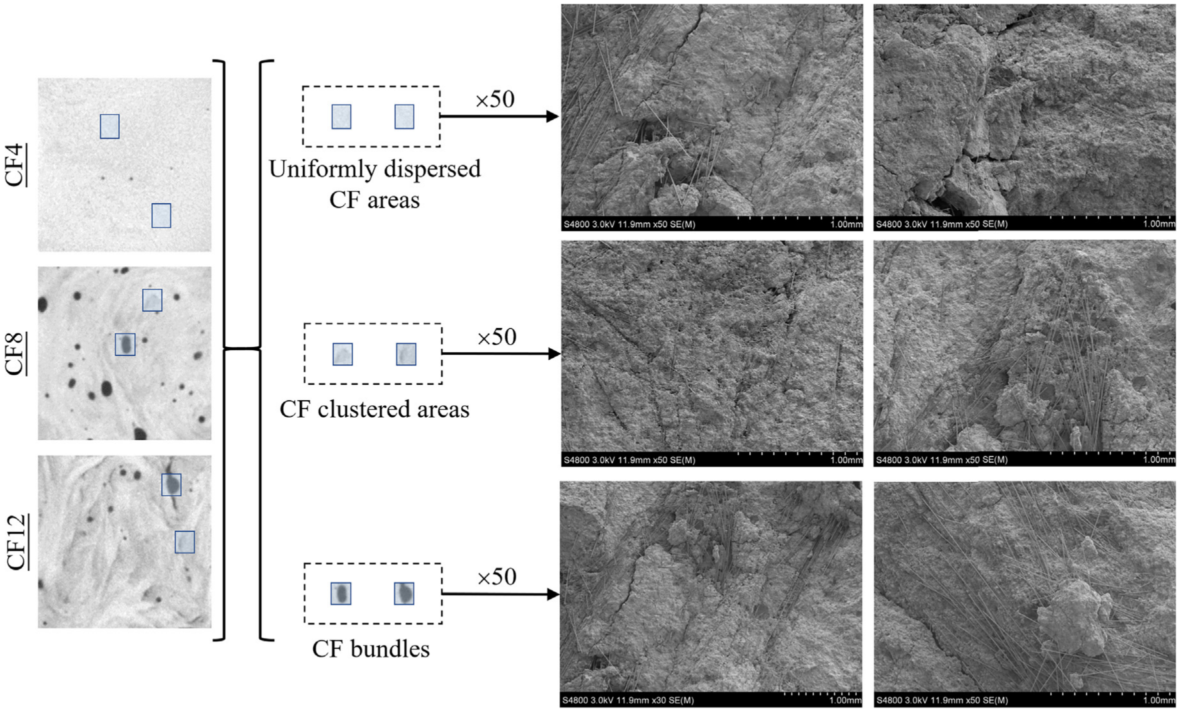

**Fig. 3.** Assistance processes for labelling using SEM images.

The schematic of the RBF network with $(n + 3)$ inputs and a scalar output is depicted in Fig. 4. The network implemented a mapping $fr$: $\boldsymbol{R}^{n+3} \rightarrow \boldsymbol{R}$ according to

$$f_r(x) = \lambda_0 + \sum_{i=1}^{n+3} \lambda_i \phi(\| \boldsymbol{x} - \boldsymbol{c}_i \|) \tag{6a}$$

$$\phi(v) = \exp\left(-\frac{v^2}{\beta^2}\right) \tag{6b}$$

where $x \in \boldsymbol{R}^{n+3}$ was the input vector; the first three elements in the input vector were the mass fraction and the resistivity of CFs, and the resistivity of the cement in the resistivity prediction, while the first three elements in the input vector were the mass fraction and the tensile strength of CFs, and the flexural/compressive strength of the cement in the prediction for the mechanical property; the rest elements were the segmentation results from the FCN; $\| \cdot \|$ denotes the Euclidean norm; $\lambda 0$, $\lambda i$, $ci$, and $\beta i$ $(i = 1,\ldots,n + 3)$ were parameters in the RBF network, which were adjusted by a forward feedback algorithm. These parameters could be regarded as different contribution of different CF morphology distribution to the resistivity of CFRC. In the forward feedback algorithm, the targets were the resistivity of the 9 specimens. The aim of the training using the forward feedback algorithm was to reduce the gap between the targets and outputs of the RBF network. Detailed information of the forward feedback algorithm for the RBF network has been introduced in the study of Sridhar and Khalil [35].

## 4. Result and discussion

### 4.1. Identification of X-ray CT images

#### 4.1.1. Overall performance of the FCN

The FCN was trained as introduced in Section 3.2. Fig. 5 presents the average binary cross entropy loss of the training and validation

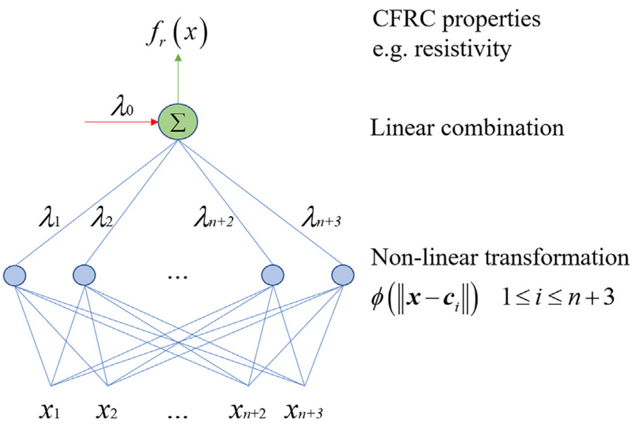

**Fig. 4.** Schematic of the RBF network.

of the FCN during the training. In Fig. 5, the change tendencies of the losses in the training and validation showed that the FCN was in the convergence to a low-loss state. The final losses of the training and validation were 0.4107 and 0.4314, respectively. It indicated that the FCN could segment CF bundles, CF clustered areas, and uniformly dispersed CF areas in the training and validation data sets precisely. Additionally, the similar final losses in the training and validation preliminarily stated that the out-of-sample accuracy and generalization ability of the trained FCN were reasonable.

To further evaluate the performance of the FCN for segmenting X-ray images, the trained model was tested by the testing data set. Table 3 present the precisions, recalls, and intersection over unions (IoUs) of the FCN in the validation and testing. Precisions, recalls, and IoUs were calculated by Eqs. (7) to (9).

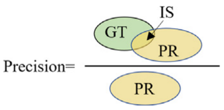

(7)

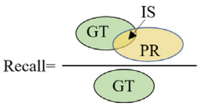

(8)

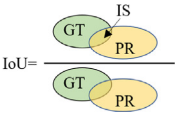

(9)

where, GT, PR, and IS were ground truth areas, prediction areas, and intersection areas of a component in an X-ray images. The data in Table 3 were averaged across all components.

In Table 3, the testing performance of the FCN was closed to the validation performance. It indicated that the FCN had a great generalization and out-of-sample ability. We could also find that the testing performance in different components was similar. It indicated that the FCN could detect CF bundles, CF clustered areas, and uniformly dispersed CF areas well. Thus, we concluded that the FCN was well-trained.

### *4.1.2. A comparison study*

The performance of the FCN was compared with another widely-used method [9] for the X-ray image segmentation. In the study of Gao et al. [9], an X-ray image was first optimized by noise filtering, edge sharpening, and contrast adjustment, then segmented by certain grayscale thresholds of different components. We named it as a grayscale-based method. X-ray images from specimens with different CF masses (0.4%, 0.8% and 1.2% of cement contents) were selected to conduct the comparison study.

Fig. 6 presents the results of the comparison study. We found that the results of the two methods in the specimens with 0.4% CF contents were similar and closed to the ground truth. However, compared with the results of the FCN, the result of the grayscale-based method in the specimens with 0.8% and 1.2% CF content was not reasonable, such as the areas in the black circle in Fig. 6. There were two reasons why the FCN had a more stable performance than the method of Gao et al: (a) In the FCN, the X-ray images were optimized by kernels with different weights, which were learned based on the ground truths. In the grayscale-based method, they were optimized by filters, whose parameters were defined by the experience of the operator; (b) In the FCN, the segmentation criterions were many feature extractors, whose parameters were given by learning the ground truths. In the grayscale-based method, the segmentation criterion was just grayscale thresholds of different components. However, the grayscale thresholds varied from one specimen to another because the density ratios of different components were various, especially

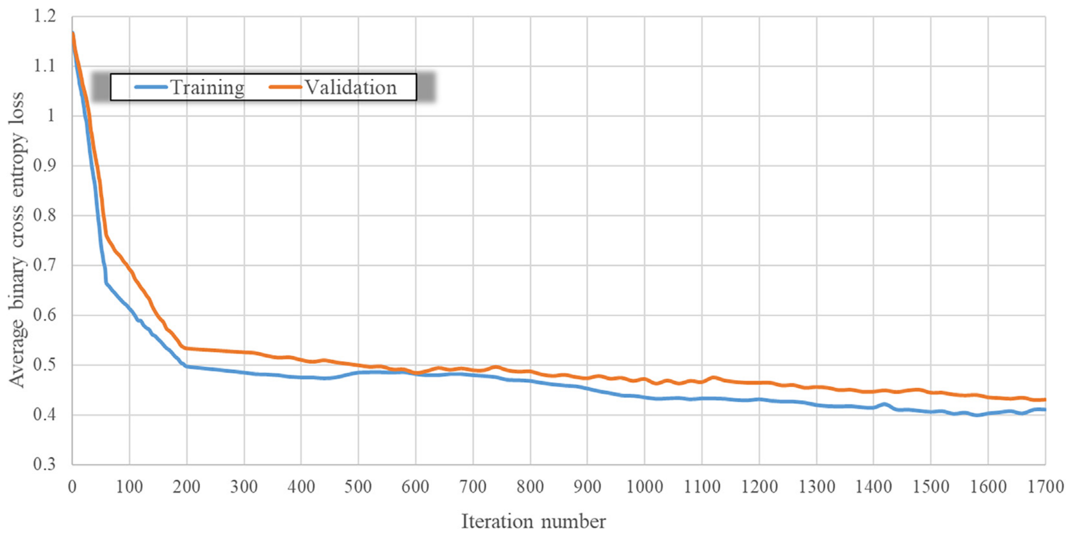

**Fig. 5.** Average binary cross entropy loss of the training and validation.

**Table 3**
Precisions, recalls, and IoUs of FCN in the training and testing (Unit: %).

| Object | Precision | | Recall | | IoU | |
|---|---|---|---|---|---|---|
| | Validation | Testing | Validation | Testing | Validation | Testing |
| CF bundles | 88.29 | 88.21 | 88.94 | 89.02 | 78.06 | 78.07 |
| CF clustered areas | 90.46 | 90.53 | 89.61 | 89.61 | 79.01 | 79.03 |
| Dispersed CF areas | 88.47 | 88.51 | 91.03 | 90.94 | 77.70 | 77.66 |
| Average results | 89.07 | 89.09 | 89.83 | 89.91 | 78.24 | 78.24 |

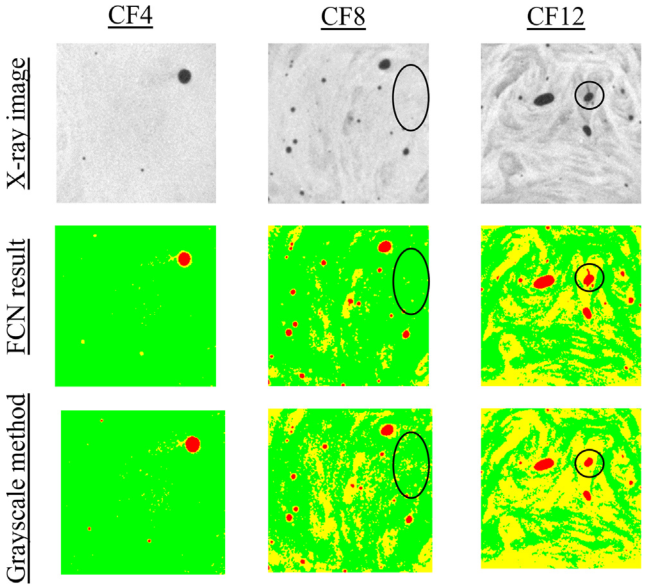

**Fig. 6.** Results of a comparison study. CF bundles, CF clustered areas, and uniformly dispersed CF areas were labeled as red, yellow, and green respectively.

the dispersed CF areas in the specimens with different CF contents. In summary, the FCN-based method provided stable and accurate segmentation results.

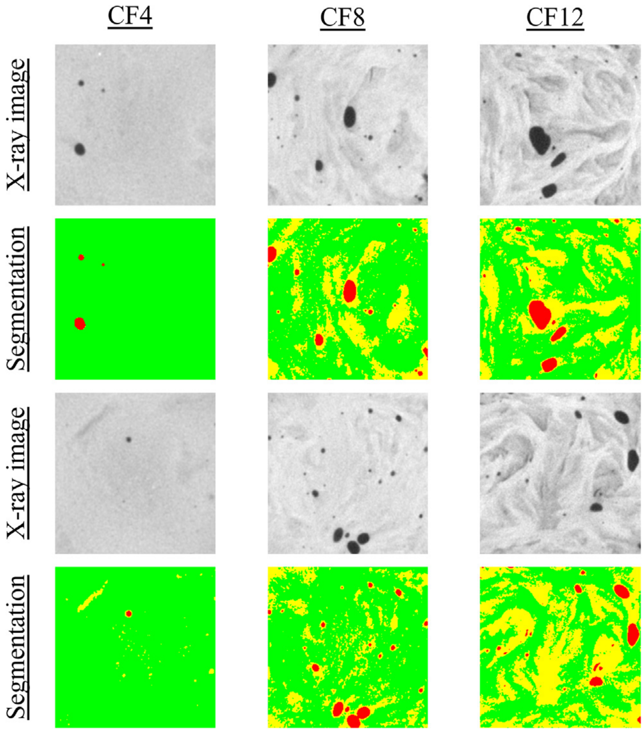

**Fig. 7.** Segmentation results by the FCN. CF bundles, CF clustered areas, and uniformly dispersed CF areas were labeled as red, yellow, and green respectively.

### 4.2. Carbon fiber morphology distribution evaluation

To analyze the effect of the CF morphology distribution, different components in the X-ray images were segmented and labeled by the well-trained FCN as shown in Figs. 6 and 7. It can be found that numbers of CF bundles, which were highly CF clustered areas, increased with the increase of the CF content. The CF clustered areas turned into continuous distribution from island-like distributions with the increase of the CF content. However, the CF dispersed areas decreased with the increase of the CF content. It indicated that more string times were necessary to make CFRC with good CF morphology distribution once the CF content was higher than 0.8%. We also found that the CF clustered areas distributed around the CF bundles. It was because that larger CF bundles cannot be dispersed into small pieces after incorporating CFs into the cement owing to the hydrophobicity of CF. Thus, CF bundles should be smashed before the incorporation to generate CFRC with good CF morphology distribution.

The CF morphology distribution changed dramatically with the increment of the CF contents. Thus, the volumes of CF bundles, CF clustered areas, and uniformly dispersed CF areas changed with various CF contents correspondingly. It was deemed as a challenging task to calculate the volumes of different components accurately owing to the drawbacks of the segmentation results in previous studies [8,9]. To solve the issue better, the segmentation results provided by the FCN were utilized for the three-dimensional (3D) reconstruction and volume calculation. The accuracies of 3D reconstruction and volume calculation depended on the identification of each component in the X-ray images [36], which was discussed sufficiently in Section 3.1.

Fig. 8 presents a part of the 3D reconstruction results of specimens with different CF contents based on the segmentation results of the FCN. The 3D reconstruction results provided visual and analyzable models where the volumes and changes of each component were clearly presented.

Table 4 presents the volume fractions of different components based on the 3D reconstruction results, which was realized by a self-developed code in the Python environment. In Table 4, we found that the CF clustered areas appeared once the CF content exceeded 0.4%. The average volume fraction of CF clustered areas in the CF12 specimens was 5.70 times higher than that in the CF4 specimens. It indicated that it was infeasible to improve the properties of CFRC simply by adding more CFs because more CF clustered areas were generated with the increase of the CF content, which had negative effects on the CFRC properties, such as stress concentration. It was important to adopt reasonable mixing methods to make sure a good CF morphology distribution in CFRC. Notably, the sum volumes of the CF bundles in CF12 were 3.712 $cm^3$, 4.019 $cm^3$, 4.147 $cm^3$, respectively, which were 133.19%, 144.99%, 149.60% volumes of the added CFs, respectively. The reason was that the CF bundles in CF12 had looser internal structures than

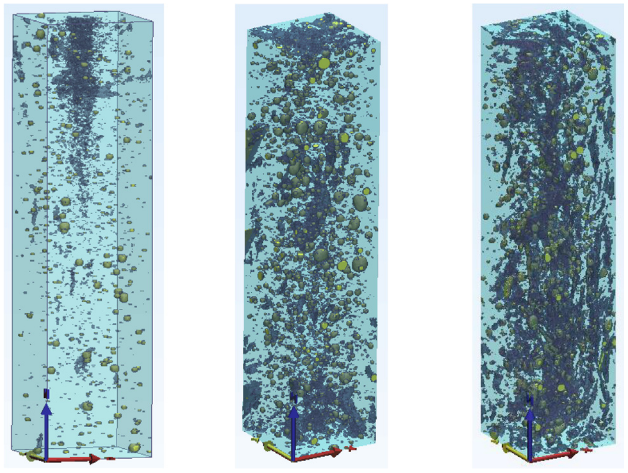

0.4% CF content 0.8% CF content 1.2% CF content

**Fig. 8.** The 3D reconstruction results for specimens based on the segmentation results of the FCN.

the added CF bundles. The looser internal structures in the CF bundles were filled with clustered CFs and air. Thus, the densities of the CF bundles in the specimens were various. It led the gray thresholds of different components in X-ray images from the CF12 specimens were different, which was a reason why the previous studies [8,9] could not provide accurate segmentation results just based on gray thresholds. Similar phenomenon could be also found in the CF clustered areas and dispersed areas.

### *4.3. Prediction for CFRC properties*

It has been proven that the different CF morphology distribution in different slides of specimens had various contributions to the CFRC properties, e.g. resistivity and mechanical property. However, the various contributions were not easy to be formulized. To provide a nondestructive and effective method to predict the CFRC properties based on the X-ray images, we proposed a cascade deep learning by combining the FCN and the RBF network. In the prediction, the 1# and 2# specimens with different CF contents were used to train the cascade deep learning, while the 3# specimens were utilized to test it. The properties of different raw materials and segmentation results were imported into the cascade deep learning as introduced in Section 3.3.

Fig. 9 presents the predicted and measured properties of the specimens with different CF contents. The average error between the predicted and measured properties of the specimens was 6.73%. It indicated that the cascade deep learning could predict the CFRC properties precisely. In Fig. 9, the specimens with the same CF contents but different morphology distribution had different resistivities and bending strengths. It indicated that the CF morphology distribution had an obvious effect on the CFRC properties, and it was not reasonable to only focus on the CF contents for the resistivity and mechanical property evaluation. The CF morphology distribution was an important factor in the performance of CFRC. For example, Fig. 10 presents $\lambda i$ ($i = 4, 5, \ldots, n + 3$) in the cascade deep learning for the prediction of the resistivity and bending strength of 2# CFRC specimen with 0.4% CF content. In an RNF, $\lambda i$ ($i = 4, 5, \ldots, n + 3$) can be used to measure the contribution of each input for the outputs [37]. In this study, $\lambda i$ ($i = 4, 5, \ldots, n + 3$) measured the contribution of different CF morphology distribution to a CFRC

**Table 4**
Volume fractions of different components (Unit: %).

| Objects | CF4 | | | | CF8 | | | | CF12 | | | |
|---|---|---|---|---|---|---|---|---|---|---|---|---|
| | 1# | 2# | 3# | Avg. | 1# | 2# | 3# | Avg. | 1# | 2# | 3# | Avg. |
| CFB | 0.11 | 0.09 | 0.08 | 0.09 | 0.73 | 0.70 | 0.61 | 0.68 | 1.45 | 1.57 | 1.62 | 1.55 |
| CFCA | 8.82 | 9.14 | 9.23 | 9.06 | 25.16 | 27.18 | 20.34 | 24.23 | 48.71 | 51.90 | 54.32 | 51.64 |
| UDCFA | 91.07 | 90.77 | 90.69 | 90.84 | 74.11 | 72.12 | 79.05 | 75.0 | 49.84 | 46.53 | 44.06 | 46.81 |

Note: CFB, CFCA, and UDCFA denotes CF bundles, CF clustered areas, and uniformly dispersed CF areas, respectively.

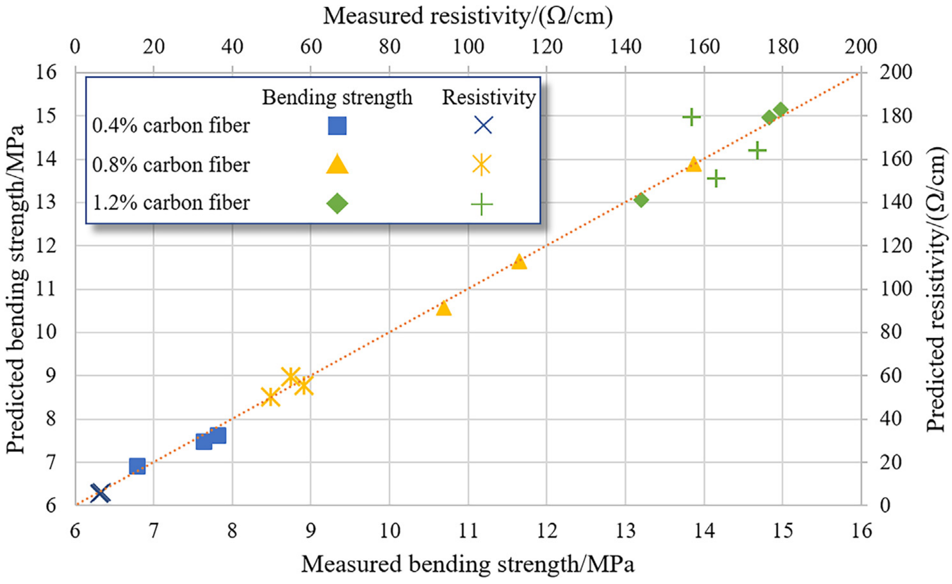

**Fig. 9.** Predicted and measured properties of specimens with different CF contents.

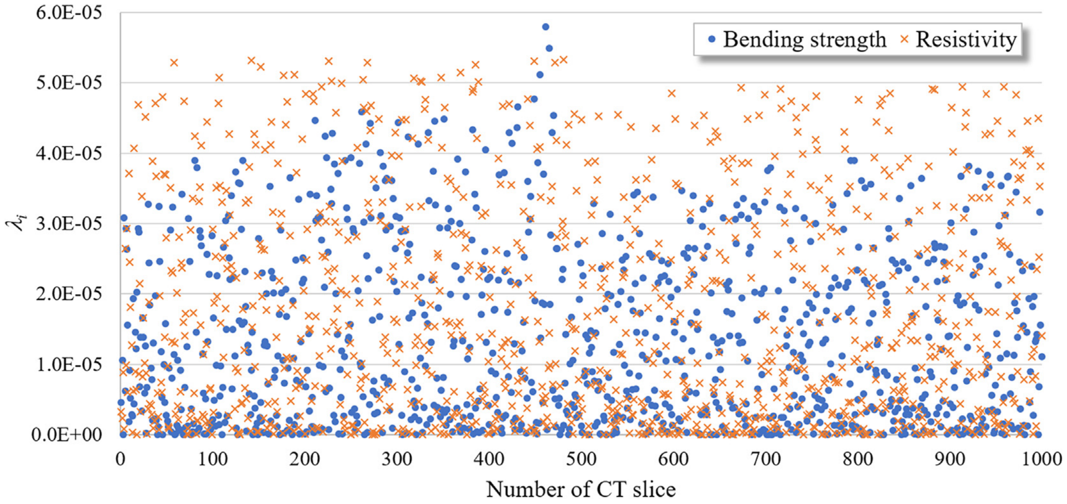

**Fig. 10.** $\lambda_i$ for the prediction of the resistivity and bending strength.

property. In Fig. 10, $\lambda i$ ($i = 4, 5, \ldots, n + 3$) varied from one to another, which indicated the CF morphology distribution in different slides had different contributions to the properties of CFRCs and $\lambda i$ ($i = 4, 5, \ldots, n + 3$) could be used to compute the contributions of the different CF morphology distribution quantificationally.

Based on the application results of the cascade deep learning, we could conclude that the proposed method could be used to predict the CFRC properties directly using X-ray scanning images. Additionally, the method could measure the different contributions of the CF morphology distribution to the CFRC properties quantificationally. Notably, the method could be extended to predict other properties of CFRC (e.g. electrical and thermal properties) based on X-ray scanning images if these properties were related to the CF morphology distribution. It provided a bridge between the CF morphology distribution and the property prediction in a nondestructive and effective mode.

## 5. Conclusions

In this work, a method using cascade deep learning and X-ray scanning was proposed to characterize the CF morphology distribution and predict CFRC properties; and the following conclusions can be drawn:

(1) The proposed method provided a stable and precisive characterization of the CF morphology distribution and prediction of CFRC properties using X-ray scanning images. The FCN-based method segmented different components in CFRC with an 89.09% average precision. The CF morphology distribution evaluation results based on the segmentation results provided visual and accurate models to calculate the volumes and changes of each component. The RBF-based method predicted the CFRC properties with a 93.27% average precision and computed the contributions of the different CF morphology distribution to CFRC properties quantificationally.

(2) The trained FCN achieved an average precision, recall, and IoU of 89.09%, 89.91%, and 78.24%, respectively, which were close to the validation results. It indicated that the FCN could segment CF bundles, CF clustered areas, and uniformly dispersed CF areas well. Additionally, the FCN had a more stable performance for the segmentation task than the traditional method.

(3) The CF morphology distribution evaluation was successfully realized using the FCN segmentation results. The 3D reconstruction results provided visual and analyzable models where the volumes and changes of each component were clearly presented. The volume calculation results show that CF clustered areas and CF bundles increased sharply with the increase of CF content, while uniformly dispersed CF areas show the opposite trend. Additionally, the CF volumes in the specimens were larger than the volumes of the added CFs owing to the looser internal structures of CF bundles, which were filled with clustered CFs and air. It led the gray thresholds of different components in X-ray images were various, which was a reason why the previous studies could not provide precise component segmentation and CF morphology distribution evaluation results.

(4) The RBF-based method provided a way to build a relationship between the CF distribution and CFRC properties and predicted the CFRC properties directly using X-ray images. The CF distribution was its real morphology distribution in the CFRC rather than the mass of CFs in a specimen. The method could also evaluate the contributions of the different CF distribution to the CFRC properties quantificationally.

## Acknowledgements

The authors gratefully acknowledge the support from Opening Foundation of Research and Development Center of Transport Industry of Technologies, Materials and Equipments of Highway Construction and Maintenance (Gansu Road & Bridge Construction Group) (No. GLKF201806). This work is also supported by Key Research and Development Program of Shaanxi Province of China (No. 2019GY-174), Co-operation Program with the UTs and INSAs (France) funded by the China Scholarship Council (No. CSC201801810108) and the Fundamental Research Funds for the Central Universities of China (Nos. 300102318402, 300102219509 and 300102319501).

## Declaration of Competing Interest

None.

## References

[1] Ryan K. Graham, Baoshan Huang, Xiang Shu, Edwin G. Burdette, Laboratory evaluation of tensile strength and energy absorbing properties of cement mortar reinforced with micro-and meso-sized carbon fibers, Constr. Build. Mater. 44 (2013) 751–756.

[2] Chuang Wang, Kezhi Li, Hejun Li, Lingjun Guo, Gengsheng Jiao, Influence of CVI treatment of carbon fibers on the electromagnetic interference of CFRC composites, Cem. Concr. Compos. 30 (6) (2008) 478–485.

[3] E. Teomete, Measurement of crack length sensitivity and strain gage factor of carbon fiber reinforced cement matrix composites, Measurement 74 (2015) 21–30.

[4] Aneeqa Masood, Zahid Shoukat, Zunaira Yousaf, Maham Sana, M. Faisal Iqbal, A.R. Rehman, I. Sultana, Aamir Razaq, High capacity natural fiber coated conductive and electroactive composite papers electrode for energy storage applications, J. Appl. Polym. Sci. 136 (13) (2019) 47282.

[5] ASTM C1229-94, Standard Test Method for Determination of Glass Fiber Content in Glass Fiber Reinforced Concrete (GFRC) (Wash-Out Test), ASTM International, West Conshohocken, PA, 2015.

[6] J. Gao, H. Guo, X. Wang, P. Wang, Y. Wei, Z. Wang, Y. Huang, B. Yang, Microwave deicing for asphalt mixture containing steel wool fibers, J. Cleaner Prod. 206 (2019) 1110–1122.

[7] D.D. Chung, Dispersion of short fibers in cement, J. Mater. Civ. Eng. 17 (4) (2005) 379–383.

[8] Zhenjun Wang, Jie Gao, Tao Ai, Wei Jiang, Peng Zhao, Quantitative evaluation of carbon fiber dispersion in cement based composites, Constr. Build. Mater. 68 (2014) 26–30.

[9] Jie Gao, Aimin Sha, Zhenjun Wang, Hu Liqun, Di Yun, Zhuangzhuang Liu, Yue Huang, Characterization of carbon fiber distribution in cement-based composites by computed tomography, Constr. Build. Mater. 177 (2018) 134–147.

[10] Jie Gao, Zhenjun Wang, Ting Zhang, Liang Zhou, Dispersion of carbon fibers in cement-based composites with different mixing methods, Constr. Build. Mater. 134 (2017) 220–227.

[11] Zhenjun Wang, Linlin Cai, Xiaofeng Wang, Xu. Chuang, Bo Yang, Jingjing Xiao, Fatigue performance of different thickness structure combinations of hot mix asphalt and cement emulsified asphalt mixtures, Materials 11 (7) (2018) 1145.

[12] M. Van Dael, P. Verboven, A. Zanella, J. Sijbers, B. Nicolai, Combination of shape and X-ray inspection for apple internal quality control: in silico analysis of the methodology based on X-ray computed tomography, Postharvest Biol. Technol. 148 (2019) 218–227.

[13] Chunfeng Lian, Su Ruan, Thierry Denœux, Hua Li, Pierre Vera, Joint tumor segmentation in PET-CT images using co-clustering and fusion based on belief functions, IEEE Trans. Image Process. 28 (2) (2019) 755–766.

[14] H. Kuang, M. Najm, D. Chakraborty, N. Maraj, S.I. Sohn, M. Goyal, M.D. Hill, A.M. Demchuk, B.K. Menon, W. Qiu, Automated ASPECTS on noncontrast CT scans in patients with acute ischemic stroke using machine learning, Am. J. Neuroradiol. 40 (1) (2019) 33–38.

[15] Yann LeCun, Bernhard E. Boser, John S. Denker, Donnie Henderson, Richard E. Howard, Wayne E. Hubbard, Lawrence D. Jackel, Handwritten digit recognition with a back-propagation network, in: Advances in Neural Information Processing Systems, 1990, pp. 396–404.

[16] Yann LeCun, Léon Bottou, Yoshua Bengio, Patrick Haffner, Gradient-based learning applied to document recognition, Proc. IEEE 86 (11) (1998) 2278–2324.

[17] Sourour Brahimi, Najib Ben Aoun, Chokri Ben Amar, Boosted convolutional neural network for object recognition at large scale, Neurocomputing 330 (2019) 337–354.

[18] Zhenjun Wang, Wu. Jiayu, Peng Zhao, Nan Dai, Zhiwei Zhai, Tao Ai, Improving cracking resistance of cement mortar by thermo-sensitive poly N-isopropyl acrylamide (PNIPAM) gels, J. Cleaner Prod. 176 (2018) 1292–1303.

[19] Guanbin Li, Yukang Gan, Wu. Hejun, Nong Xiao, Liang Lin, Cross-modal attentional context learning for RGB-D object detection, IEEE Trans. Image Process. 28 (4) (2019) 1591–1601.

[20] Alberto Castillo, Siham Tabik, Francisco Pérez, Roberto Olmos, Francisco Herrera, Brightness guided preprocessing for automatic cold steel weapon detection in surveillance videos with deep learning, Neurocomputing 330 (2019) 151–161.

[21] Wenqi Ren, Jingang Zhang, Xu. Xiangyu, Lin Ma, Xiaochun Cao, Gaofeng Meng, Wei Liu, Deep video dehazing with semantic segmentation, IEEE Trans. Image Process. 28 (4) (2019) 1895–1908.

[22] D. Palani, K. Venkatalakshmi, An IoT based predictive modelling for predicting lung cancer using fuzzy cluster based segmentation and classification, J. Med. Syst. 43 (2) (2019) 21.

[23] Mingjie Xu, Shouliang Qi, Yong Yue, Yueyang Teng, Xu. Lisheng, Yudong Yao, Wei Qian, Segmentation of lung parenchyma in CT images using CNN trained with the clustering algorithm generated dataset, Biomed. Eng. Online 18 (1) (2019) 2.

[24] Shanwen Zhang, Wenzhun Huang, Harry Wang, Lesion detection of computed tomography and magnetic resonance imaging image based on fully convolutional networks, J. Med. Imaging Health Inf. 8 (9) (2018) 1819–1825.

[25] Xiangming Zhao, Laquan Li, Lu. Wei, Shan Tan, Tumor co-segmentation in PET/CT using multi-modality fully convolutional neural network, Phys. Med. Biol. 64 (1) (2018) 015011.

[26] Hai Liu, Aimin Sha, Zheng Tong, Jie Gao, Autonomous microscopic bunch inspection using region-based deep learning for evaluating graphite powder dispersion, Constr. Build. Mater. 173 (2018) 525–539.

[27] Ruijin Cang, Hechao Li, Hope Yao, Yang Jiao, Yi Ren, Improving direct physical properties prediction of heterogeneous materials from imaging data via convolutional neural network and a morphology-aware generative model, Comput. Mater. Sci. 150 (2018) 212–221.

[28] Jiwang Jiang, Zhen Zhang, Qiao Dong, Fujian Ni, Characterization and identification of asphalt mixtures based on Convolutional Neural Network methods using X-ray scanning images, Constr. Build. Mater. 174 (2018) 72–80.

[29] GB175-2007, Standards of Common Portland Cement in China, General Administration of Quality Supervision, Inspection and Quarantine of the People's Republic of China, Beijing, 2007.

[30] Yuanxia Yang, Methods study on dispersion of fibers in CFRC, Cem. Concr. Res. 32 (5) (2002) 747–750.

[31] Yoshua Bengio, Deep Learning, Convolutional Networks, http://www.iro.umontreal.ca/-bengioy/dlbook/.

[32] Benjamin Graham, Fractional max-pooling, arXiv preprint arXiv:1412.6071 (2014).

[33] Matthew D. Zeiler, Rob Fergus, Stochastic pooling for regularization of deep convolutional neural networks, arXiv preprint arXiv:1301.3557 (2013).

[34] Jonathan Long, Evan Shelhamer, Trevor Darrell, Fully convolutional networks for semantic segmentation, in: Proceedings of the IEEE conference on computer vision and pattern recognition, 2015, pp. 3431–3440.

[35] Sridhar Seshagiri, Hassan K. Khalil, Output feedback control of nonlinear systems using RBF neural networks, IEEE Trans. Neural Networks 11 (1) (2000) 69–79.

[36] Tetsuya Suzuki, Tomoki Shiotani, Masayasu Ohtsu, Evaluation of cracking damage in freeze-thawed concrete using acoustic emission and X-ray CT image, Constr. Build. Mater. 136 (2017) 619–626.

[37] Sheng Chen, Colin F.N. Cowan, Peter M. Grant, Orthogonal least squares learning algorithm for radial basis function networks, IEEE Trans. Neural Networks. 2 (2) (1991) 302–309.